energies

MDPI

Article

Experimental and Numerical Investigation on the Dynamics of Impacting Droplet Spreading at Small Weber Numbers

Ning Wang [1], Jiqing Zhang [2] and Zhenyu Zhang [1,*]

[1] School of Mechanical Engineering, Beijing Institute of Technology, Beijing 100081, China
[2] China International Engineering Consulting Corporation, Beijing 100048, China
* Correspondence: zhenyu.zhang@bit.edu.cn; Fax: +010-68913637

Abstract: The dynamic of droplet spreading on a free-slip surface was studied experimentally and numerically, with particularly interest in the impacts under relatively small droplet inertias ($We \leq 30$). Our experimental results and numerical predictions of dimensionless droplet maximum spreading diameter β_{max} agree well with those of Wildeman et al.'s widely-used model at $We > 30$. The "1/2 rule" (i.e., approximately one half of the initial kinetic energy E_{k0} finally transferred into surface energy) was found to break down at small Weber numbers ($We \leq 30$) and droplet height is non-negligible when the energy conservation approach is employed to estimate β_{max}. As *We* increases, surface energy and kinetic energy alternately dominates the energy budget. When the initial kinetic energy is comparable to the initial surface energy, competition between surface energy and kinetic energy finally results in the non-monotonic energy budget. In this case, gas viscous dissipation contributes the majority of the dissipated energy under relatively large Reynolds numbers. A practical model for estimating β_{max} under small Weber numbers ($We \leq 30$) was proposed by accounting for the influence of impact parameters on the energy budget and the droplet height. Good agreement was found between our model predictions and previous experiments.

Keywords: fuel droplet spreading; small weber numbers; maximum spreading diameter; energy dissipation; Modeling

Citation: Wang, N.; Zhang, J.; Zhang, Z. Experimental and Numerical Investigation on the Dynamics of Impacting Droplet Spreading at Small Weber Numbers. *Energies* **2022**, *15*, 8181. https://doi.org/10.3390/en15218181

Academic Editors: Gholamreza Kefayati and Hasan Sajjadi

Received: 20 September 2022
Accepted: 27 October 2022
Published: 2 November 2022

1. Introduction

Droplet impact on a solid surface is regularly observed in many nature and industrial process, such as raindrops hitting soil [1,2], petrochemical processes [3,4], ice resisting [2,5], painting [6], fog harvesting [7] and spray combustion in various engines [8–10]. As for port-injection gasoline engines, hydrocarbon fuel droplet impacts on the intake port and intake valves tend to form an oil film and therefore facilitate fuel evaporation; while for direct-ignition engines, liquid fuel is more likely to impact the combustion chamber due to the increasingly high fuel injection pressure [11]. It has been recognized that spray/wall interaction characteristics substantially influence mixture formation and subsequent combustion, and therefore influences engine efficiency and emission. One of the most important issues of spray/wall interaction is the dynamic of a droplet impacting a solid surface, which is usually adopted to estimate the wall film performance [12–15].

As a fundamental phenomenon in the investigation of spray/wall interactions, the dynamic of a droplet impacting a solid surface has been studied for decades. Previous investigations indicate that the impacting dynamic is controlled by the impact Weber number $We = \rho_l D_0 U_0^2/\sigma_l$, and the Reynolds number $Re = \rho_l D_0 U_0/\mu_l$. In some cases, the Reynolds number can be replaced by the Ohnesorge number $Oh = \mu_l/\sqrt{\rho_l \sigma_l D_0}$, since $Oh = \sqrt{We}/Re$. Where D_0 is the droplet initial diameter, U_0 is the impact velocity, and ρ_l, μ_l, and σ_l, are the droplet density, viscosity and surface tension, respectively.

By employing dimensionless parameters, transitions between different impacting outcomes such as spreading, bouncing and splashing can be quantified. For droplet spreading, one of the most important factors is the dimensionless droplet maximum spreading diameter β_{max}, which is defined as the ratio of droplet maximum spreading diameter D_m over its initial diameter D_0, and which yields $\beta_{max} = D_{max}/D_0$. Quantifying β_{max} is useful in many practical applications, such as estimating oil film characteristics [12].

A considerable number of models have been proposed for β_{max} quantifying, which have been reviewed in some excellent literature [16–18]. Normally, the existing models for predicting β_{max} possess three different categories, namely, scaling law [11,16,19–29] momentum conservation [30–33] and energy conservation [17,34–41]. For viscous fluid such as liquid hydrocarbon fuel, the contribution of viscous dissipation on energy conservation is non-negligible therefore an energy conservation approach tends to predict more accurate β_{max}. In this case, accurately predicting the viscous dissipation rate, and hence the dissipated kinetic energy, is essential for predicting droplet dynamic characteristics.

To account for viscous dissipation during spreading, Wildeman et al. proposed the "1/2 rule" which indicates that around one half of the kinetic energy finally transforms into surface energy for droplet spreading on an ideal free-slip surface under relatively large Weber numbers ($We > 30$) and Reynolds numbers. The "1/2 rule" allows a complete theoretical solution for β_{max} prediction. The uniform droplet deformation under relatively large We may be the main reason for uniform kinetic energy dissipation and the asymptotically accurate "pizza-shaped" deformation for $We > 30$ indicates droplet inertia dominates droplet internal flow, almost regardless of Re. In this case, liquid viscosity slightly influences droplet spreading dynamic. In spite of these advances in understanding droplet spreading dynamic under large Weber numbers ($We > 30$), it is surprising to find that only a few works have been conducted for small Weber numbers ($We \leq 30$).

It is recognized that, in the combustion chamber of modern energy conversion devices such as an internal combustion engine, the increasingly higher ambient pressure together with the complex air motion, substantially reduces the inertia of the fuel droplets and implies that droplets are more likely to impact the chamber edge at small Weber numbers [42]. To investigate droplet spreading under relatively small We, Qin et al. [43] experimentally studied the dynamic of a glycerol-water blend droplet impact on a near-smooth stainless steel surface. They observed the non-monotonic effect of liquid viscosity on β_{max} at $We = 13$ and 30. Specifically, an increase of liquid viscosity promotes energy dissipation under relatively small Re cases, however, viscosity plays an opposite role under relatively large Re conditions. Subsequently, Zhang and Zhang [44] numerically simulated Qin et al.'s experiments, numerically confirmed the non-monotonic tendency of β_{max} and attributed it to the dual role of liquid viscosity under small Weber numbers ($We \leq 30$), where droplet deformation is non-uniform.

It has been recognized that droplet shapes at maximum deformation instant τ_{max} will change from "puddle-shaped" to "pizza-shaped" when droplet inertia increases from $We = 3$ to $We = 30$. Most of the previous studies have focused on modeling β_{max} under large We, where droplet deformation appears as uniform "pizza-shaped" styles and hence energy dissipation is We-independent. In terms of the complex droplet deformation and energy dissipation characteristics, modeling β_{max} under relatively small We has been investigated insufficiently [45,46].

Based on the discussion stated above, the present study aims to experimentally and numerically investigate the impacting dynamics and model β_{max} under relatively small Weber numbers ($We \leq 30$). Following our previous numerical works [44,47,48], a well-validated front tracking method (referred to as FTM hereinafter) was employed to conduct the numerical simulations associated with our experiments. In the following text, we shall first introduce our experimental and numerical approach in Section II, followed by the discussion of spreading dynamic, particularly for small Weber numbers.

Subsequently, the correlation between impact parameter and β_{max} will be discussed. Finally, the conclusion will be presented in the last section.

2. Experimental Setup and Numerical Methodology

2.1. Experimental Setup

Figure 1 shows the schematic of our experimental apparatus. A Gyger Smld 300 G droplet generator (1) was mounted on the top side of the constant volume chamber (2), which was filled with atmospheric pressure nitrogen. Nitrogen was initially stored in the cylinder and entered into the chamber through the regulating valve (3). Liquid fluid was deposited in the liquid tank (4) and driven by high pressure nitrogen to form the droplet. The droplet impact on the solid surface (5) process was recorded by a Photron Fastcam Nova S12 high-speed camera (6) with 100,000 fps, and an LED lamp (7) was used for backlight. Specifically, the angle between camera and the solid surface was set as 15° to better display the result and all measured quantities in the vertical direction, such as height and speed, were conducted with a cosine correction of 15°. For the repeatability of the experiments, the sphericity of the droplet can be quantified by $S = min\,(D_H/D_V\,, D_V/D_H)$, where D_H and D_V are the droplet sizes measured in the horizontal and vertical directions respectively (D_H is the value after a cosine correction of 15°). S is 1.0 ± 0.05, indicating a satisfactory and reproducible droplet sphericity. Meanwhile, a typical droplet initial diameter is 2.75×10^{-4}m and the typical Oh is around 0.007. As for uncertainty estimation, the maximum error in the estimated droplet diameter is approximately 1 pixel (equivalent to 6.16 μm). Therefore, the uncertainty in D_0 and U_0 is less than 2.5%. As a result, the relative error of the Weber number $\Delta We/We = \Delta D_0/D_0 + 2\,\Delta U_0/U_0$ is less than 7.5%. The distance between the outlet of the droplet generator to the solid surface is around 50 mm and this distance can vary to avoid droplet vibration. The droplet has a non-zero and variable initial velocity at the outlet of the droplet generator. A self-developed program based on video-image processing has been used to realize droplet recognition, droplet diameter, velocity extraction and the impact parameters calculation during the spreading dynamics. Before each experiment, a smooth stainless-steel surface was cleaned carefully three times with anhydrous ethanol until the surface was free of any stains and of any scratches on the surface. When performing the experiment, the surface was placed directly below the outlet of the droplet generator, high-speed camera trigger mode was set to end and droplet generator 'peak-hold' related parameters were set at the same time. The high-speed camera was triggered manually to start recording images and the droplet generator was triggered to produce droplets. The recording image was stopped as soon as any droplets impacted the surface. The surface can be rotated to move the area that has not been impacted by droplets underneath the outlet for the next experiment. When the surface was full of water stains, the clean surface was replaced and the experiment was repeated.

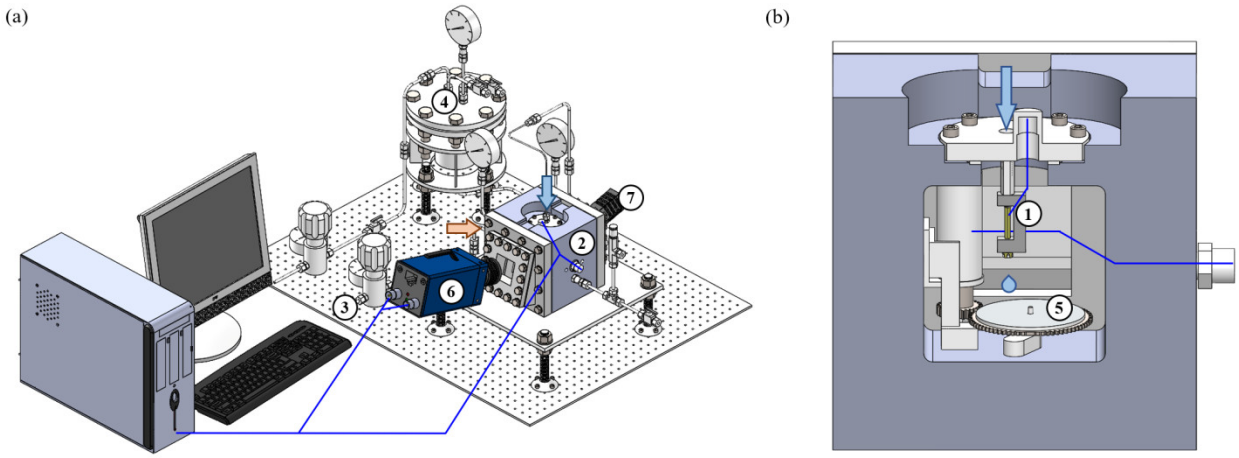

Figure 1. (**a**) Schematic diagram of the experimental setup for the droplet impact at elevated ambient pressures and (**b**) sectional view of the pressure vessel where the experimental equipment or pipeline corresponded to the serial number. (1) Droplet generator, (2) constant volume chamber, (3) regulating valve, (4) liquid tank, (5) solid surface, (6) high-speed camera, and (7) LED lamp. In (**a**), the orange arrow represents the injection of high-pressure compressed nitrogen into the chamber and the blue arrow represents the liquid supply into droplet generator respectively. The blue solid line represents the path for electrical signals and data.

2.2. Numerical Methodology

The present numerical study was conducted by adopting the FTM, which was originally developed by Unverdi et al. [49]and Tryggvason et al. [50] to simulate droplet impacts on a free-slip surface for incompressible two-phase flow. A second-order centered difference scheme for the spatial variables and an explicit first order time integration method was employed to solve the governing equations of both liquid and gas phases, given by

$$\nabla \cdot \boldsymbol{U} = 0 \tag{1}$$

$$\frac{\partial(\rho \boldsymbol{U})}{\partial t} + \nabla \cdot (\rho \boldsymbol{U}\boldsymbol{U}) = -\nabla p + \nabla \cdot \mu[\nabla \boldsymbol{U} + (\nabla \boldsymbol{U})^T] - \sigma \int \kappa \boldsymbol{n} \delta(\boldsymbol{x} - \boldsymbol{x_f}) dA \tag{2}$$

where $\boldsymbol{U}$ is the velocity vector, ρ is the density, p is the pressure, μ is the viscosity, σ is the surface tension coefficient, κ is twice the mean curvature of local field, $\boldsymbol{n}$ is the unit vector outwardly normal to the local front. The term δ is the constructed three-dimensional δ function which represents the singular force, surface tension, over the phase interface, $\boldsymbol{x}$ is the point at which the equation is evaluated, and $\boldsymbol{x_f}$ is a point on the front.

The FTM solves a single set of conservation equations with appropriate interface terms in the whole field with a Eulerian coordinate grid and tracks liquid–gas interfaces using a Lagrangian approach. Figure 2 shows the computational domain of the current numerical simulation. In the cylindrical coordinate, z-axis is structured by the droplet initial velocity normal to the surface, while the r-axis is perpendicular to the droplet initial velocity. Axisymmetric boundary condition is specified for the z-axis, while free-slip boundary conditions are specified to all of the other boundaries including the impacting solid surface.

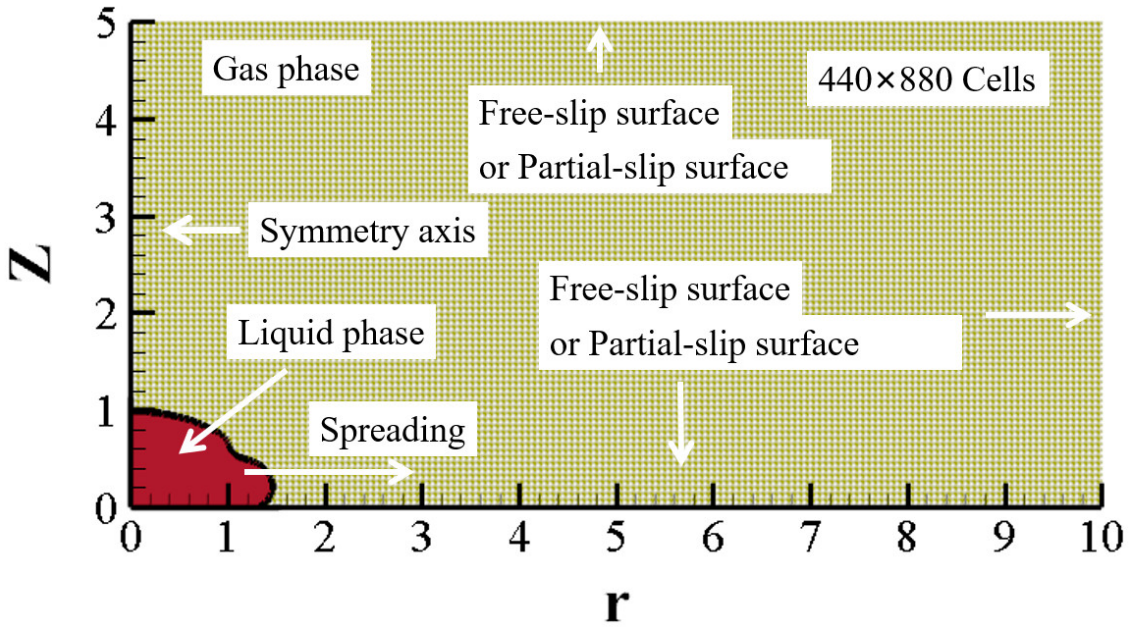

Figure 2. Axisymmetric computational domain with uniform structured grids. Each unit length contains 88 cells. The boundary conditions can be set to a free-slip or partial-slip surface as illustrating in the graph.

The computational domain of width $10R_0$ and height $5R_0$ is discretized by a uniform orthogonal mesh with 440×880 cells, which means each unit length contains 88 grid points. Grid-dependence of the present numerical approach has been fully checked in many previous works in which FTM is not sensitive to the grid size because the liquid–gas interface is tracked by the Lagrangian particles rather than computational cell. Additionally, the present cell size has been validated in one of the author's previous publications, where simulations with the same cell size have been proved to successfully and accurately solve the droplet problems. It should be noted that the droplet impact problem is always involved in complex gas film problems. In order to simplify the present simulation, we only focus on the limiting condition of droplet spread with a gas film throughout the whole process.

Governing equations are nondimensionalized by the droplet radius $R_0 = D_0/2$, initial velocity U_0, and droplet density ρ_l. Time is normalized by using $\tau = t \cdot U_0/D_0$, where t is the real time. In addition, several previous studies [44,47,48] have confirmed that gas-liquid density ratio ρ_g/ρ_l and viscosity ratio μ_g/μ_l are two or three orders of magnitude smaller than unity. Therefore, their effects on droplet deformation and viscous dissipation can be neglected, where ρ_g and μ_g are gas density and viscosity, respectively. Meanwhile the droplet initial kinetic energy is $E_{k0} = \pi\rho V_0^2 D_0^3/12$ and the droplet initial surface energy is $E_{s0} = \sigma\pi D_0^2$.

3. Results and Discussion

3.1. Comparison between Experimental Results and Numerical Predictions

The FTM adopted in the present study has been sufficiently applied and validated in many previous studies [44,47,48,51–58] on droplet dynamic problems. For a brief summary, Pan et al. [54] and Zhang and Zhang [48] numerically simulated the binary droplet collision dynamics using FTM, numerical predictions show good agreement with experimental results. Subsequently, one of the authors compared their numerical result of droplet spreading on a free-slip surface to Pan et al.'s experiment and very good agreement in terms of instantaneous droplet shape was observed, which again demonstrates that the present numerical method can be used to accurately predict the evolution of droplet deformation during impacting. Additionally, the present numerical approach successfully reproduced, albeit qualitatively, the experimental observation of Qin et al. [43] where β_{max} varies non-monotonically with the liquid viscosity (characterized by the Oh).

To further validate the numerical calculation, ultra-pure water droplet impacts on a smooth surface were achieved by our experimental system and numerical calculation, respectively. For the mentioned characteristics of the surface used in the current experiment in Table I, the droplet corresponds to spreading on a partial slip boundary surface and with an advancing contact angle between 90° and 180°. For our current experimental work, our numerical calculation employs a simplified boundary condition where partial slip boundary and a fixed contact angle 180° are used instead of advancing contact angles between 90° and 180° as in the experiments.

Figure 3 shows the time sequences of droplet spreading process for both experimental and numerical results under four different conditions. For spreading at $We = 30$ and $Re = 750$, as shown in Figure 3a, $\tau = 0$ indicates the time instant when the droplet just contacts the surface. As time develops to $\tau = 0.224$, a rim-shaped bulge is squeezed out due to sufficiently large initial kinetic energy, which is 2.5-times the initial surface energy. Subsequently, spreading begins and the rim moves outwardly then reaches its maximum spreading at $\tau = 1.234$, when the droplet deforms to a thin liquid film with a thicker annular rim with a pizza-like shape. A similar phenomenon also can be seen for $We = 21$ and $Re = 612$, where the initial kinetic energy is 1.75-times the initial surface energy, as shown in Figure 3b. However, the rim thickness seems higher than that of the $We = 30$ case. With impact, inertia degenerates to $We = 10$, where initial kinetic energy is weaker than that of surface energy. Droplet at the maximum spread time instant of $\tau = 0.62$ hardly keeps its pizza-like shape, but tends to transfer into a donut-like shape, as shown in Figure 3c. The donut-like shape droplet becomes more prominent in the case of the relatively smaller Weber number, as shown in Figure 3d. When compared to the numerical predictions, regardless of some discrepancies to be discussed later, good agreement can be observed for the geometric features in which the spherical droplet turns concave and the rim is squeezed out.

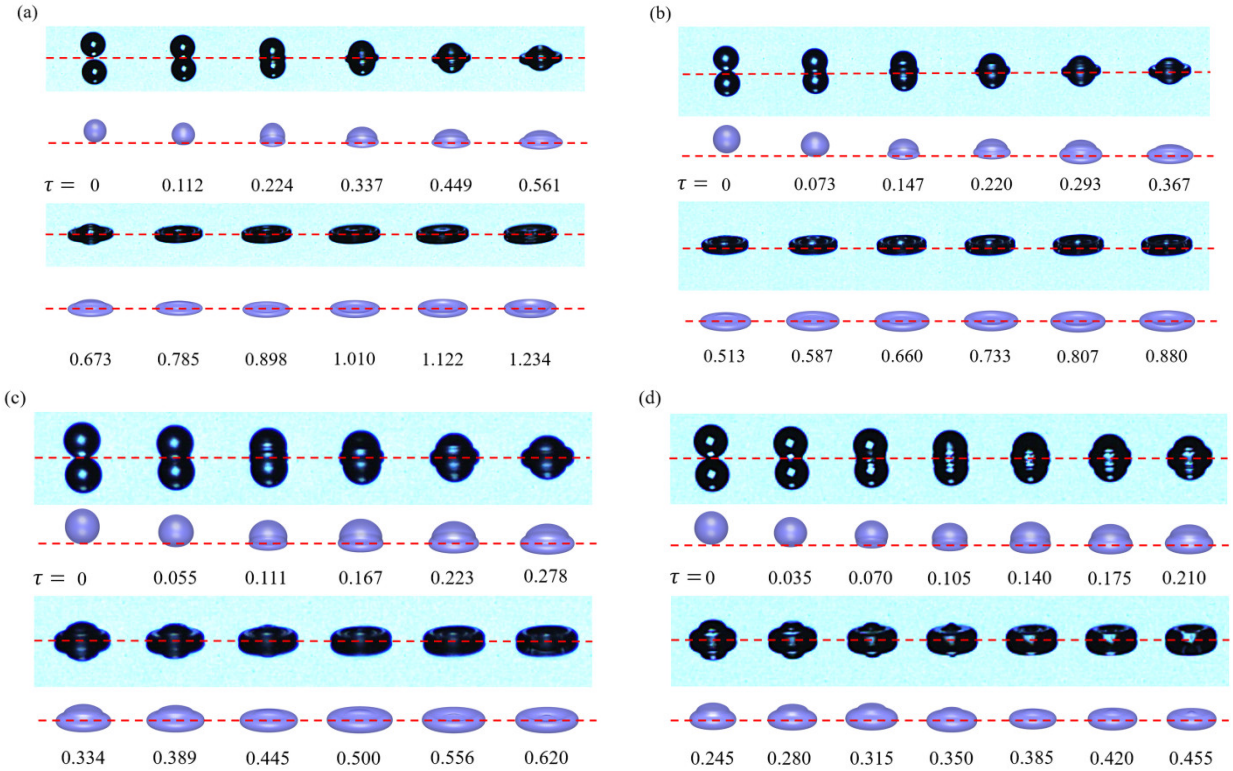

Figure 3. Time sequences of ultra-pure water droplet impact a stainless-steel smooth surface arrayed in non-dimensional time τ under (**a**) $We = 30$ and $Re = 750$, (**b**) $We = 21$ and $Re = 612$, (**c**) $We = 10$ and $Re = 421$, (**d**) $We = 5$ and $Re = 281$ under atmospheric pressure for experimental and numerical results. The red dash line denotes the impact horizontal line.

More supporting evidence for validation is illustrated in Figure 4 where droplet non-dimensional diameter D/D_0 varied with non-dimensional time τ. Our numerical predictions agree very well with the experimental results under the condition of $We = 30$ and $Re = 750$, as shown in Figure 4a, but some discrepancies in the earlier stage of our numerical simulation tends to underestimate the non-dimensional diameter. The moderate difference of the droplet shape in Figure 3b–d can be understood by recognizing that the simplified boundary conditions for the numerical calculation cause the slight deviations corresponding to the real physics for droplet spreading. Beyond this, numerical predictions again coincide with the experimental results. Consequently, it is confirmed that the present numerical approach can accurately predict the evolution of droplet spreading during impacting a free-slip surface.

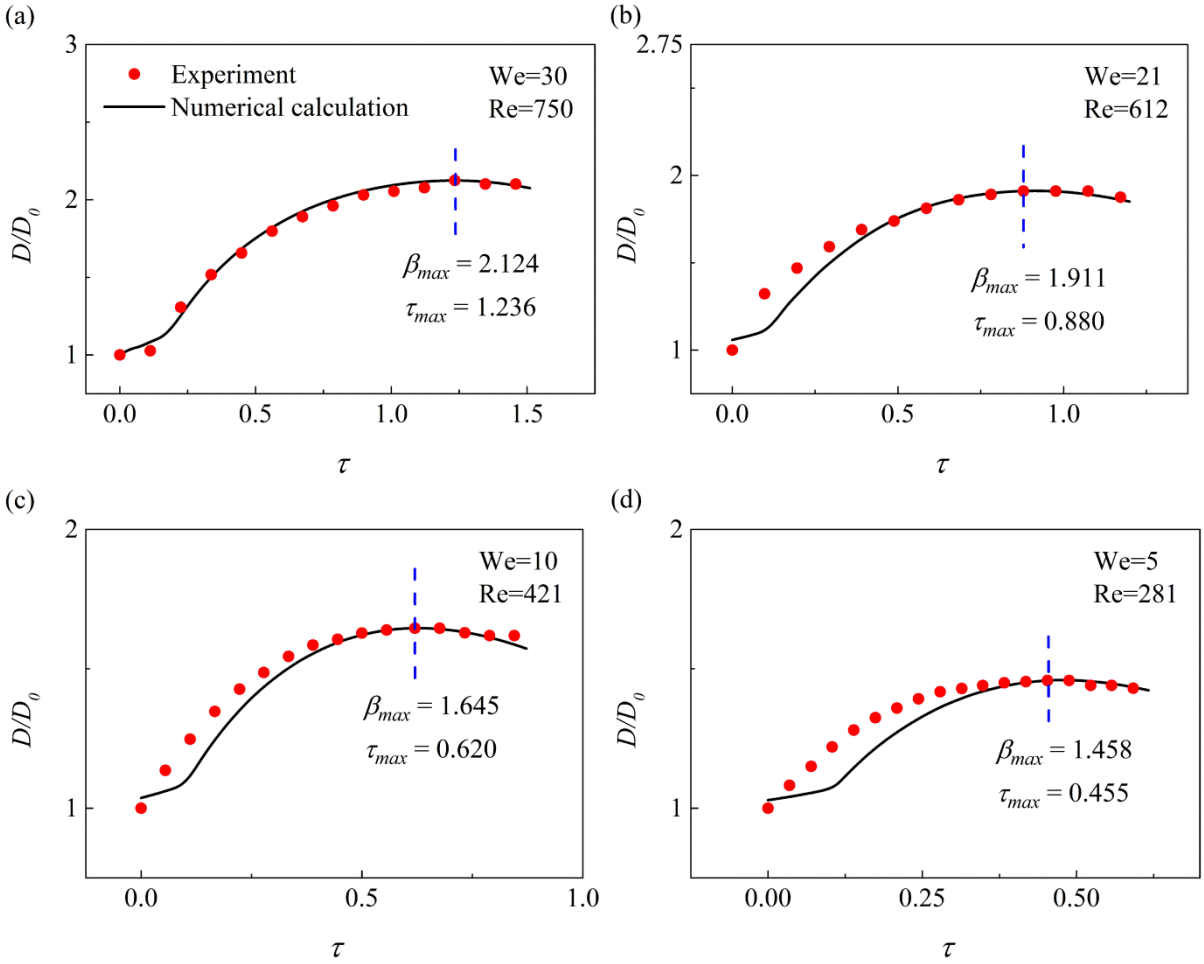

Figure 4. Comparison between the numerical calculation (denoted by the black solid line) and the experiment results (denoted by the red solid point) for the droplet non-dimensional diameter D/D_0 varied with non-dimensional time τ under 4 groups of impact parameters. (**a**) $We = 30$ and $Re = 750$, (**b**) $We = 21$ and $Re = 612$, (**c**) $We = 10$ and $Re = 421$, (**d**) $We = 5$ and $Re = 281$.

3.2. Droplet Spreading under Relatively Large Weber Numbers ($We > 30$)

To further validate our numerical simulation, we first simulated droplet spread on the free-slip surface under relatively large Weber numbers, the results were compared to the widely-used model of Wildeman et al. [40] model, given by

$$\beta_{max} = \sqrt{\frac{4}{1-\cos\theta}\left(\frac{We}{24}+1\right)} \quad (3)$$

which is estimated based on the energy conservation approach where the initial kinetic energy E_{k0} ($E_{k0} = \pi\rho V_0^2 D_0^3/12$) is equal to the sum of dissipation energy E_d, left-over kinetic energy E_k and surface energy increment ΔE_s at max deformation instant τ_{max}, yields

$$E_{k0} = E_d + E_k + \Delta E_s \quad (4)$$

Our numerical simulation considers the limiting condition to be droplet spread with a gas film, which is progressively close to the contact angle $\theta = 180^{\circ}$. Therefore, Figure 5 shows the comparison between our present experiments (denoted by the stars), numerical simulations (denoted by the dots) and the prediction of Wildeman et al.'s model (denoted by the solid lines) for β_{max} under relatively large Weber numbers ($We \geq 30$). Moreover, the experimental results of Tran et al. [27] are also plotted in this figure for a comparison. In addition, the experimental data in current work and cited in predecessors are summarized in Table 1.

Table 1. Summary of cited and current experiment data.

Cited from	Impact Parameter	Experimental Detail	Surface Property and Contact Angle θ
Tran et al. [27]	We = 4.95~29.2	Milli-Q water (1 atm air) D_0 = 1.7 and 2.2 mm (typically)	Leidenfrost droplet (Gentle film boiling) $\theta = 180°$
Pan et al. [54]	We = 2.25 and 2.27	Tetradecane (1 atm air) D_0 = 107.2 and 170.6 μm	head-on equivalent binary droplet collision $\theta = 180°$
Tang et al. [11]	We = 1.04~3.37	Tetradecane (1 atm air) $D_0 = 120\mu$m (typically)	head-on equivalent binary droplet collision $\theta = 180°$
Current experiment	$We = 5, Re = 281$ $We = 10, Re = 421$ $We = 21, Re = 612$ $We = 30, Re = 750$	Ultra-pure water (1 atm air) density $\rho_l = 998\ kg/m^3$ viscosity μ_l = 1.005 m$Pa \cdot s$ surface tension σ = 71.99 mN/m $D_0 = 275\ \mu$m (typically)	Stainless-steel Surface roughness $R_a = 0.1\ \mu$m Static contact angle $\theta_s = 50°$

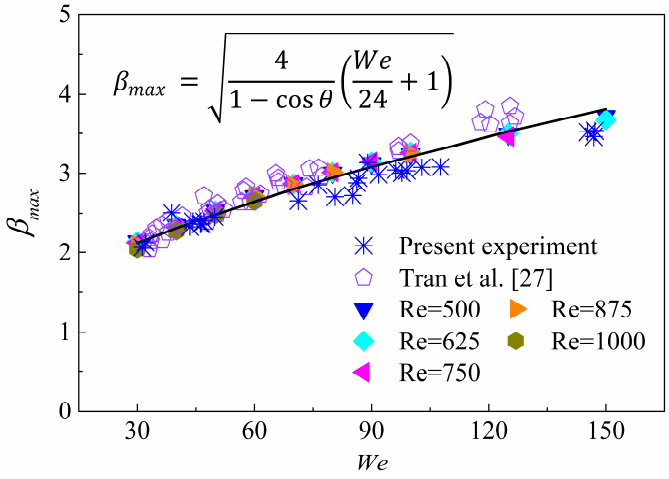

Figure 5. Comparison between the present experimental results (denoted by the stars), Tran et al.'s experimental results (denoted by the pentagon symbols) [27] and numerical predictions (denoted by the solid symbols) and the Wildeman et al.'s model (denoted by the solid line) for dimensionless droplet maximum spreading diameter β_{max} under large Weber numbers ($We \geq 30$).

Very good agreement again appears between our numerical results and the predictions of Wildeman et al. Our predictions show that β_{max} is generally *Re*-independent for relatively large Reynolds numbers ($Re \geq 500$), once again, consistent with the tendencies of previous investigations [40,42].

Since Wildeman et al.'s model is estimated according to the energy conservation approach associated with the "1/2 rule", we subsequently show the energy budget in Figure 6, in which all the energies were normalized by the initial kinetic energy E_{k0} and therefore the sum of E_k, E_d and ΔE_s is the unity. To further investigate the viscous dissipation characteristics, we counted the energy dissipation in both liquid phase (denoted by E_{dl}) and gas phase (denoted by E_{dg}), and therefore $E_d = E_{dl} + E_{dg}$. The "1/2 rule" is also indicated in each graph.

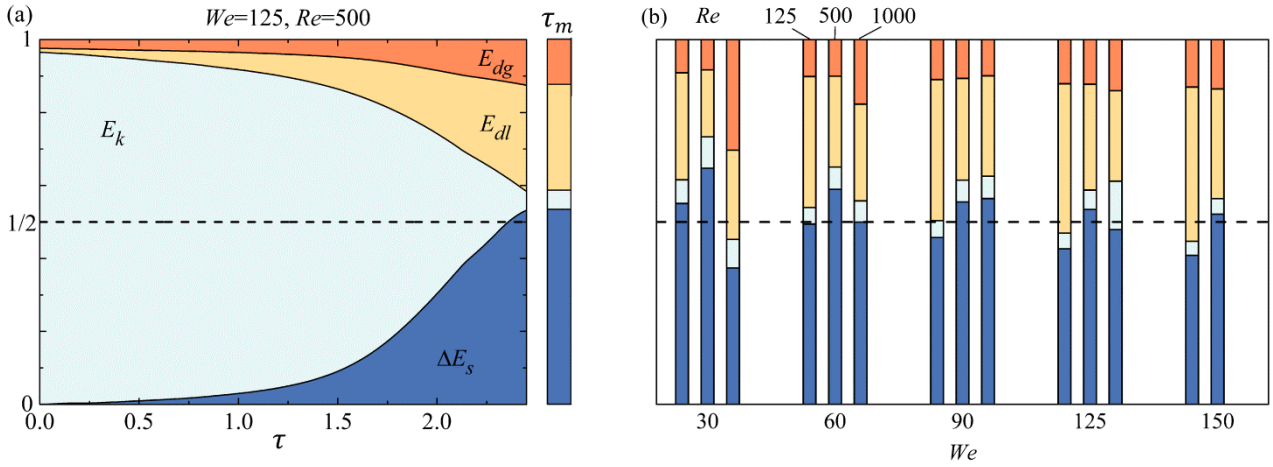

Figure 6. Energy budget of droplet spread on the free-slip surface under We ≥ 30. The dash line indicates the "1/2 rule". (**a**) the evolution of four different energies during droplet spreading process and (**b**) shows the energy budget at τ_{max} for various droplet inertias and Reynolds numbers.

Figure 6a shows the evolution of four different energies during the droplet spreading process, while Figure 6b shows the energy budget at τ_{max} for various droplet inertias and Reynolds numbers. In this case we defined $\tau = 0$ as the time instant when the droplet just contracts the surface. The initially non-zero E_d at $\tau = 0$, shown in Figure 6a, can be attributed to the slight deformation together with the droplet moving-induced gas motion, and results in the viscous dissipation in either liquid or gas phases before droplet-wall contracting. The pre-dissipated energy is around 3% of the initial kinetic energy E_{k0} and slightly influences the energy budget, so that it can therefore be ignored in the present study. For energy budget shown in Figure 6b, all the predictions generally follow the "1/2 rule". Although viscous dissipation in the liquid phase contributes more to E_d, viscous dissipation in the gas phase, i.e., E_{dg} still cannot be ignored.

It is recognized that energy dissipation originates from the viscous dissipation during droplet deformation, therefore droplet spread time scale plays a relatively considerable role in influencing β_{max}. Wildeman et al. assumed that τ_{max} is proportional to the β_{max} and suggested $\tau_{max} = \beta_{max} - 1$ for droplet spread on both free- and no-slip surfaces. Consequently, the correlation between β_{max} and τ_m for our predictions under large Weber numbers is shown in Figure 7. It is obvious that τ_{max} and β_{max} meet the quantitative relationship ($\tau_{max} = \beta_{max} - 1$) quite well, and hence confirms the accuracy of our numerical simulation.

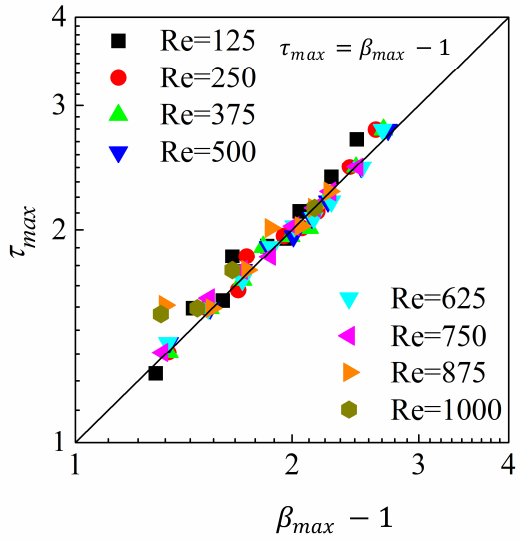

Figure 7. Spreading time τ_{max} versus maximum spreading diameter β_{max} for simulations with $We \geq 30$.

3.3. Droplet Spreading under Relatively Small Weber Numbers ($We \leq 30$)

Figure 8 shows the prediction of β_{max} under small Weber numbers ($We \leq 30$). Again, the solid line indicates Wildeman et al.'s model, while the experimental results of Pan et al., Tang et al., Tran et al. [27] and the present case are also shown in the figure for a comparison.

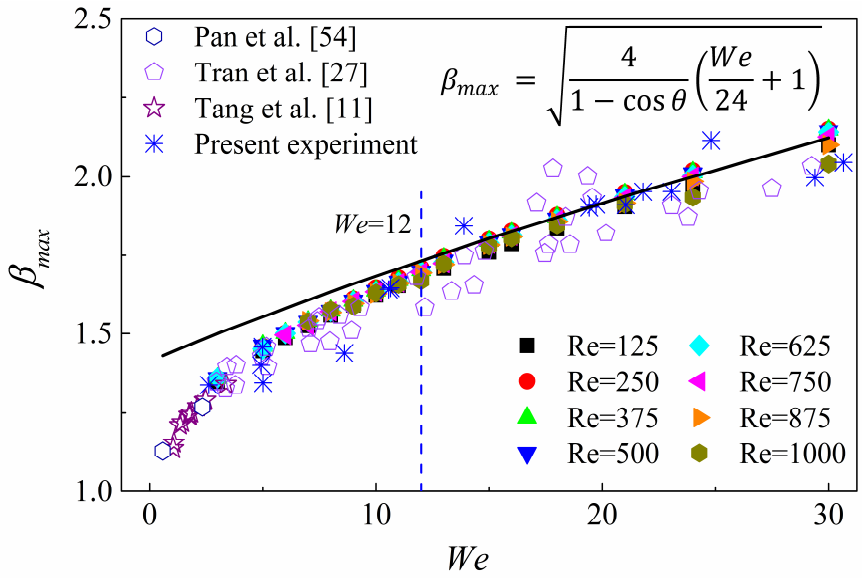

Figure 8. Comparison between the present experimental results (denoted by the stars), Tang et al.'s experimental results (denoted by the pentagram symbols) [11], Tran et al.'s experimental results (denoted by the pentagon symbols) [27], Pan et al.'s experimental results (denoted by the hexagon symbols) [54], numerical predictions (denoted by the solid symbols) and the Wildeman et al.'s model [40] (denoted by the solid line) for dimensionless droplet maximum spreading diameter β_{max} under small Weber numbers ($We \leq 30$).

It is seen for both experimental results and the numerical predictions that β_{max} slightly deviates from Wildeman et al.'s model as droplet inertia decreases from $We = 30$ to around $We = 12$, below which the predicted β_{max} substantially deviates from the model of Wildeman et al. This deflection can be attributed to the breakdown of the "1/2

rule" and the dominant factor of energy budget transfer from kinetic energy to the surface energy, to be elucidated in the following text. It should be noted that β_{max} is determined by the energy conversion during droplet spreading. For Wildeman et al.'s model, there are two important hypotheses i.e., around one half of the initial kinetic energy transfers into surface energy and droplet shape at τ_m can be regarded as a "pizza-shaped" disk, whose thickness can be ignored when compared to the spreading diameter.

To investigate the reason why droplet spreading under small Weber numbers deviates from the model of Wildeman et al., we show the energy budget for $We \leq 30$ in Figure 9. It is clearly seen that the "1/2 rule" breaks down and ΔE_s increases with Weber number decreasing, indicating an We-dependent energy budget. Normally, dissipation energy (sum of E_{dg} and E_{dl}) moderately decreases as We decreases. ΔE_s that is generally larger than 1/2 indicates that surface energy may play a dominant role in droplet deformation during droplet spreading [44].

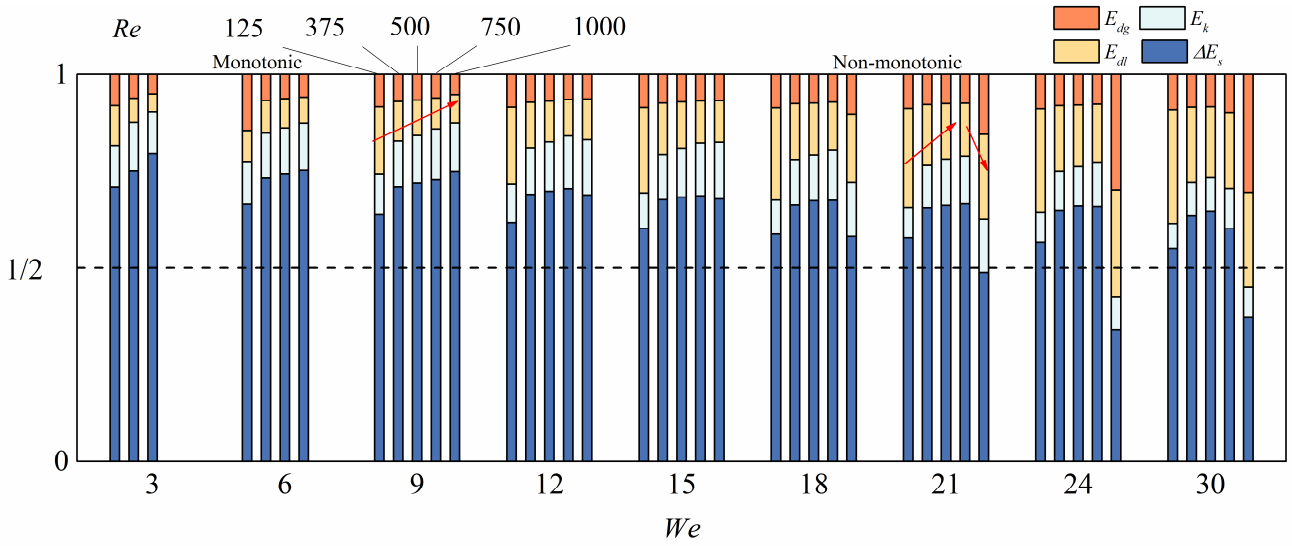

Figure 9. Energy budget under small Weber numbers for different Reynolds numbers.

An interesting observation for different We cases is that ΔE_s decreases monotonically as Re increases when the $We < 12$; however, it changes non-monotonically when the $12 \leq We \leq 30$. This observation corresponds to the previous experimental observation of Qin et al. and the numerical simulation of our previous investigation [44], in which they attributed the non-monotonic trend as the dual role of liquid viscosity under intermediate droplet inertias, however, the underlying physics have not been fully explained.

To further explore the dual role of liquid viscosity, we first counted the energy dissipation in both liquid (denoted by E_{dl}) and gas phase (denoted by E_{dg}). In case of the droplet spreading under intermediate Weber numbers, such as $We = 30$, E_{dl} first decreases then moderately increases as Re increases. However, E_{dg} tends to keep steady under relatively large Reynolds numbers then increases substantially as Re further increases.

To unravel the underlying physics responsible for the observation state above, we respectively calculated the local viscous dissipation rate in liquid and gas phases as

$$\Phi = \mu f(\dot{\boldsymbol{\gamma}}) = 2\mu\left[\left(\frac{\partial u}{\partial r}\right)^2 + \left(\frac{u}{r}\right)^2 + \left(\frac{\partial w}{\partial z}\right)^2\right] + \mu\left(\frac{\partial u}{\partial z} + \frac{\partial w}{\partial r}\right)^2 - \frac{2\mu}{3}\left[\frac{1}{r}\frac{\partial (ru)}{\partial r} + \frac{\partial w}{\partial z}\right]^2 \quad (5)$$

here, $\dot{\boldsymbol{\gamma}}$ is the strain rate tensor, u is the velocity component in the r–direction, w the velocity component in z–direction. Subsequently, the overall viscous dissipation rate (VDR) was obtained by integrating the local viscous dissipation rate Φ over the

computational domain, while VDR in liquid phase and gas phase were calculated by integrating Φ over the droplet and the ambient gas.

Figure 10 shows the time-dependent viscous dissipation rate (VDR) for droplet impacts under two different Weber numbers. For spreading with relatively small inertia ($We = 9$), as shown in Figure 10a–c, the lowest Reynolds number ($Re = 125$) generally produces highest overall VDR, most of which is contributed by the liquid viscous dissipation. As the Reynolds number increases to $Re = 750$, overall VDR monotonically decreases because the increase of Re actually decreases liquid viscosity (characterized by the Ohnesorge number $Oh = \sqrt{We}/Re$). As Reynolds number further increases to $Re = 1000$, VDR in the earlier stage decreases, however, it produces a substantial "bulge" as time develops, which results in the VDR in turn being larger than smaller Re cases ($Re = 375 - 750$) in an appropriate time period. However, this reversion is insufficiently strong to influence the energy dissipation tendency. The "bulge" can be attributed to the dual role of liquid viscosity, which has been primarily discussed in the previous investigations [42,44]. Although the majority of the VDR is contributed by the liquid phase, the "bulge" can also be seen in the gas phases, indicating that the dual role of liquid viscosity influences energy dissipation in both liquid and gas phase.

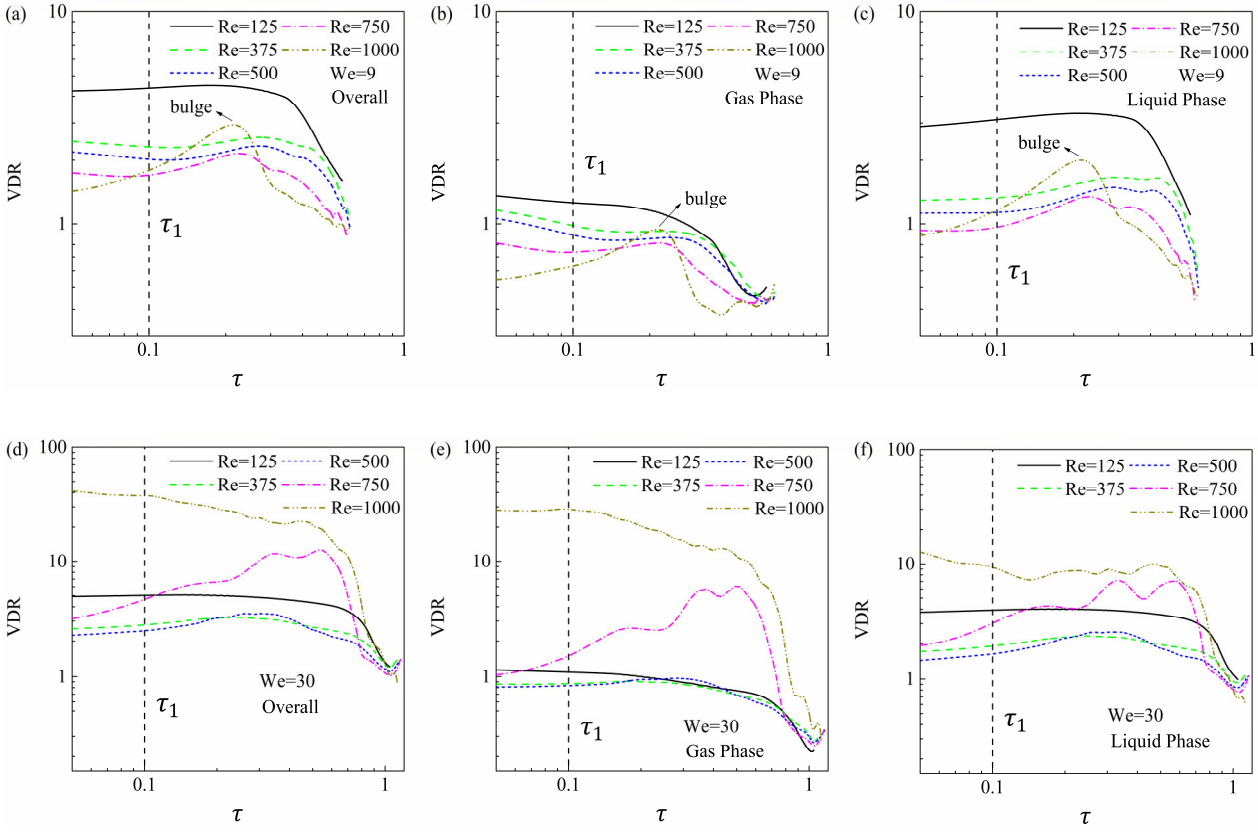

Figure 10. Viscous dissipation rate for droplet spread under different Re cases at (**a**–**c**) $We = 9$ and (**e**–**f**) $We = 30$.

Figure 10d,e accounts for $We = 30$ that overall VDR decreases as Reynolds number increases from $Re = 125$ to 500 because a decrease in liquid viscosity reduces viscous dissipation. In this case viscous dissipation in the liquid phase contributes the majority of the overall VDR. However, as Re continually increases to 750 and finally 1000, the dual role of liquid viscosity is sufficiently strong to influence an energy dissipation tendency in which overall VDR substantially increases. The contribution of gas viscous dissipation

gradually increases and in turn dominates the energy dissipation at $Re = 1000$, and therefore produces a non-monotonic energy budget, as shown in Figure 9.

To further show the flow motion and viscous dissipation characteristics in both liquid and gas phases, we integrated the local viscous dissipation rate Φ as

$$VDR(r) = \int_0^h \Phi dz \tag{6}$$

where h is the computational domain height (as shown in Figure 2). Figure 11 compares the $VDR(r)$ (on the left Y-axis) and droplet shape (denoted by interface on the right Y-axis) for $We = 9$ and 30 cases at the characteristic time instant τ_1 (indicated in Figure 10).

For spreading at $We = 9$, shown in Figure 11a, all three $VDR(r)$ curves increase rapidly from droplet center to rim (with r increasing), the peak value, which decreases as Re increases, appears around the droplet rim where a large stain rate can be found. This can be attributed to the fact that, in the very earlier stage when the droplet just contacts the surface, a rim is just squeezed out and therefore induces a relatively high strain rate. Consequently, we show the local strain rate $f(\dot{\gamma})$ distribution in the near-rim area in each graph for a better understanding. It seems that increasing the Re slightly influences the $f(\dot{\gamma})$ in both liquid and gas phases, because in this case surface energy dominates the energy budget and therefore produces a similar strain rate. Increasing peak $VDR(r)$ results from the increase of liquid viscosity, which dominates the viscous dissipation under relatively small droplet inertia ($We = 9$). As Weber number increases to $We = 30$, shown in Figure 11b, Re again slightly influences the $f(\dot{\gamma})$ in the liquid phase, therefore $VDR(r)$ increases as Re increases. However, relatively large Re produces substantially higher $f(\dot{\gamma})$ in the gas phase near the rim, which in turn dominates viscous dissipation and results in a substantially high gas viscous dissipation. Consequently, the dissipation energy is mainly powered by the viscous dissipation in the gas phase under high Re condictions. These can be attributed to the reason that, for droplet spread under intermediate inertia ($12 \leq We \leq 30$), the unconsumed kinetic energy transfer from liquid phase to the gas therefore induced substantially high strain rate in the gas phase, hence substantial gas viscous dissipation and E_{dg}.

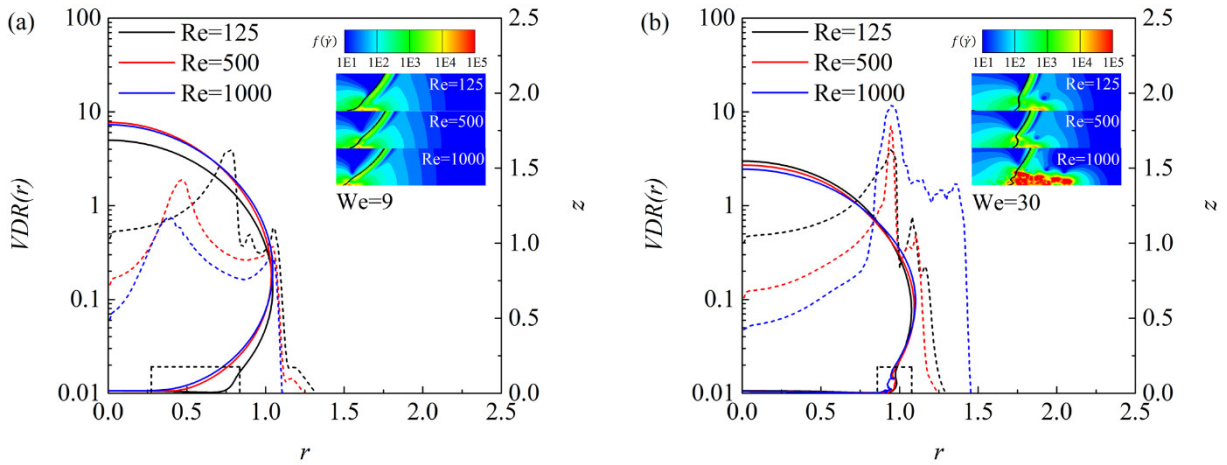

Figure 11. Comparison of $VDR(r)$ for droplet spreading under three different Reynolds numbers for (**a**) $We = 9$ and (**b**) $We = 30$.

To understand the observation stated above, we first recognized that $We = 12$ indicates that droplet initial kinetic energy ($E_{k0} = \pi\rho V_0^2 D_0^3/12$) is equal to the initial surface energy ($E_{s0} = \sigma\pi D_0^2$), therefore droplet surface energy dominates the energy budget for $We < 12$ and produces similar strain rate Φ in both liquid and gas phases, and hence

viscosity dominates the energy dissipation, which decreases as Re increases (a.k.a., liquid viscosity decreasing).

For $12 \leq We \leq 30$ the energy transfer could be more complex. When Re is relatively small, most of the droplet kinetic energy can be consumed in the very earlier stage and therefore surface energy dominates the energy budget. In this case, surface force suppresses droplet deformation and viscous dissipation is controlled by the liquid viscosity, so that dissipated energy decreases as Re increases. However, for relatively large Re, initial kinetic energy is unable to be consumed in a timely manner, which results in the kinetic energy still dominating the energy budget and droplet deformation being improved as Re increases. Therefore, energy dissipation is controlled by the strain rate which is promoted by increasing Re, hence results in the increasing energy dissipation. Consequently, a non-monotonic tendency can be observed under intermediate Weber numbers.

3.4. Droplet Deformation Transitions

Another significant factor that should be considered is the non-negligible droplet height under small Weber numbers ($We \leq 30$). In this study we employed three different heights to characterize droplet shape, namely, droplet center height h_c, throat height h_t and rim height h_r. Figure 12a illustrates the comparison of two impact morphologies during droplet spreading for cases under large and small We with puddle- and pizza-shaped droplet, respectively. Figure 12b shows the evolution of three heights with increasing impact Weber number and the Reynolds number fixed at $Re = 1000$. Overall, all three heights decrease as Weber number increases because increasing impact inertia promotes droplet spreading outwardly and therefore results in an increasingly thinner liquid film. However, droplet deformation shows a complex tendency and can be divided into three distinct regimes as impact Weber number increases, namely, puddle-shaped regime (I), transition regime (II) and pizza-shaped regime (III).

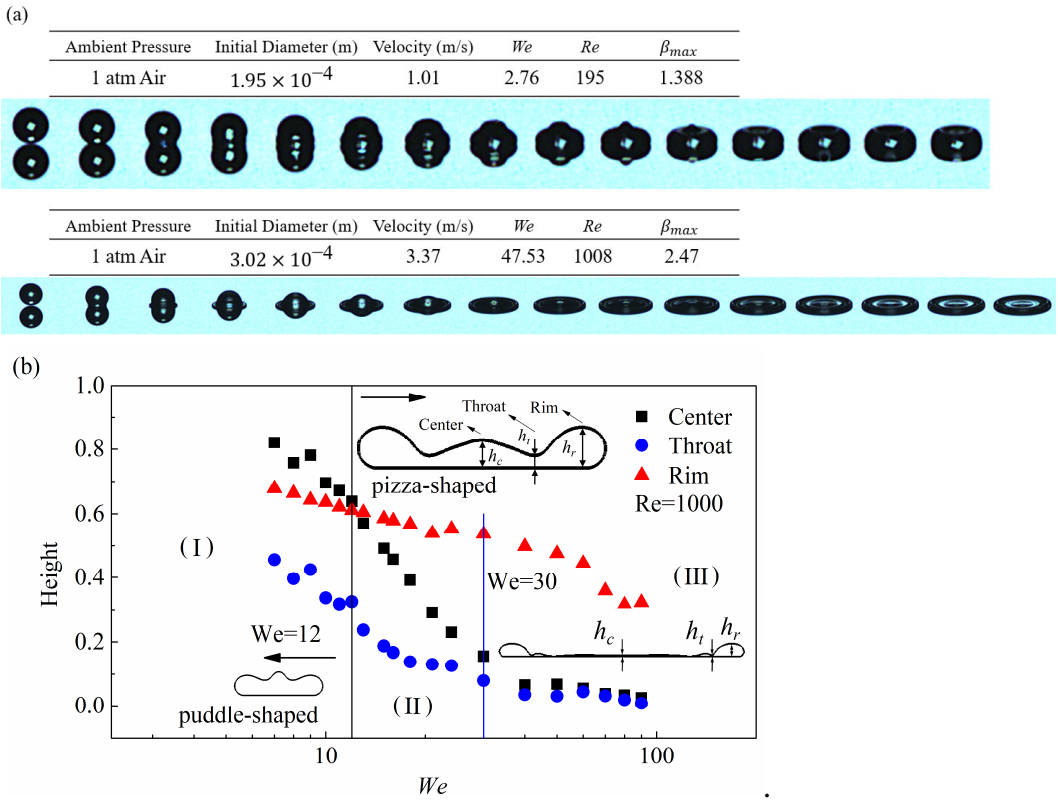

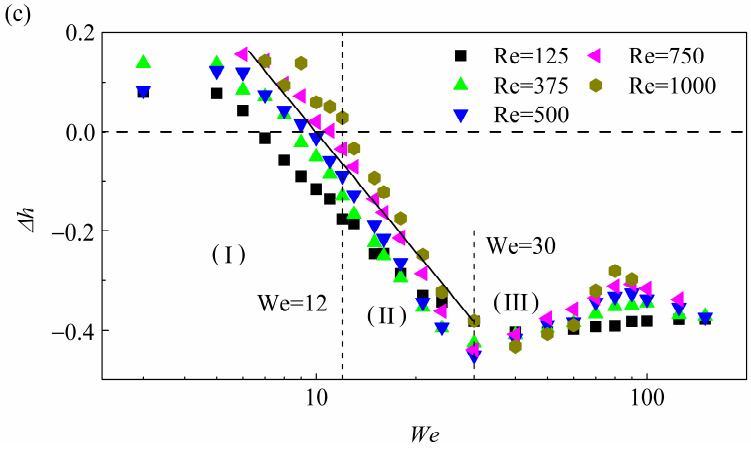

Figure 12. Schematic of droplet deformation transition characterized by different heights. (**a**) Comparison of droplet morphology at τ_{max} between droplet impact under small *We* ($We = 2.76$) and large *We* ($We = 47.53$), (**b**) three different heights h_c, h_t and h_r varying with We and (**c**) the difference between h_c and h_r i.e., Δh varying with We.

For relatively smaller Weber number ($We < 12$) in regime (I), it seems h_c shows the highest value among three heights while h_t shows the lowest, indicating that a relatively small impact inertia results in a droplet that appears like a puddle with a flattened top and a rounded edge. As droplet inertia increases to regime (II), the initial kinetic energy gradually dominates the energy transfer so that a rim can be squeezed out from the bottom part of the droplet and a narrow neck throat is formed to connect the rim and the central part of the droplet; the droplet shape is close to a pizza but with a thick height. As droplet impact inertia continually increases and finally reaches beyond $We = 30$, i.e., regime (III), we found h_c approaches h_t and its evolution becomes steady, indicating that the droplet deformation has become more pronounced so that a thin lamella is bordered by a rim; the droplet height can then be ignored when estimating the surface energy.

To further show the transition of droplet deformation, we quantitatively compared the relationship between droplet center height h_c and the rim height h_r denoted as $\Delta h = h_c - h_r$, as shown in Figure 12c. When the droplet spreading is in regime (I), i.e., $We < 12$, initial kinetic energy is insufficiently strong to overcome the constraints of surface tension, hence Δh is generally larger than zero where cases under smaller Re are not taken into consideration. As droplet inertia increases into regime (II), Δh decreases linearly by $We = 30$, beyond which droplet spread in the regime (III) and Δh tends to become steady, indicating a uniform droplet deformation. These again suggest why the model of Wildeman et al. works well under $We > 30$ in regime (III), where droplet height is negligible when compared to the spreading diameter and is associated with the "1/2 rule", β_{max} can be accurately estimated according to energy conservation. However, as We decreases to regime (II) ($12 \leq We \leq 30$) although the "1/2 rule" breaks down, the pizza-shaped droplet is precariously maintained, therefore β_{max} only slightly deviates from Wildeman et al.'s model. As We further decreases to $We < 12$, droplet deformation transitions into puddle-shape regime (I), where droplet height is non-negligible when estimating β_{max}, and therefore produces substantial deflection.

3.5. Modeling β_{max} under Small Weber Numbers

It has been recognized in the previous section that the "1/2 rule" breaks down when the droplet impact inertia decreases to $We \leq 30$, therefore β_{max} gradually deviates from the model of Wildeman et al. The deviation could be more prominent when the $We < 12$, where surface energy rather than kinetic energy dominates the energy budget, results in the non-negligible height. Therefore, in this section, we first adopted a revised Weber number We_r, which is defined as the droplet initial kinetic energy ($E_{k0} = \pi\rho V_0^2 D_0^3/12$) over its initial surface energy ($E_{s0} = \sigma\pi D_0^2$) hence $We_r = We/12$. The We_r has been

employed by Zhang and Zhang [44] to precisely measure the relative importance between droplet initial kinetic energy and surface energy.

To estimate β_{max} using an energy conservation approach, we first introduced the droplet deformation ratio R_d as the rate of surface energy increment ΔE_s to initial kinetic energy E_{k0}, given by $R_d = \Delta E_s / E_{k0}$. Figure 13 is used to show the relationship between R_d and droplet revised Weber number We_r. Regardless of droplet spreading under relatively large Re cases for $We_r > 1.0$, to be discussed later, R_d seems independent of the Re and the simulation results agree well with the fitted formula, given by

$$R_d = 0.7We_r^{-0.1} \tag{7}$$

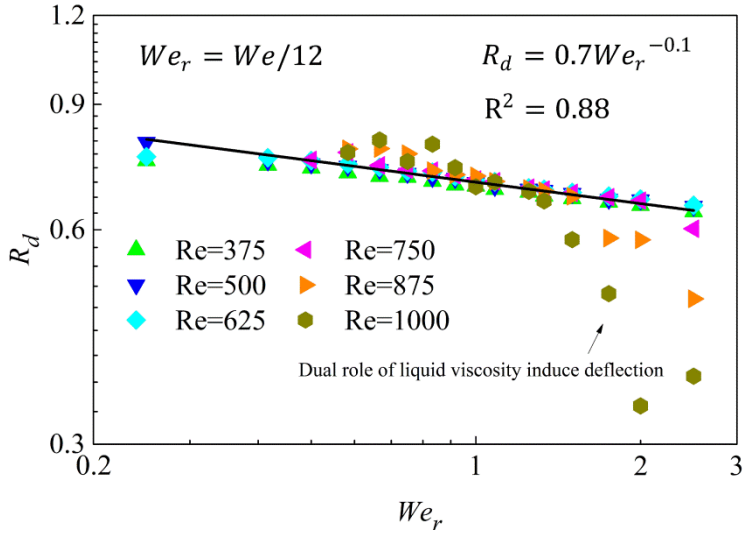

Figure 13. Correlation between $R_d = \Delta E_s / E_{k0}$ and revised Weber number with $R^2 = 0.88$.

Moderate deviation under $We_r > 1.0$ for relatively large Re cases can be attributed to the dual role of liquid viscosity in producing additional viscous dissipation which as discussed in the previous section III B. In this case, surface energy increment can be express as $\Delta E_s = R_d \cdot E_{k0}$. Meanwhile, cases under smaller Re are not the emphasis of the analysis in the current work and these data points are not used in the fitting for energy ratio R_d in order to obtain a matching and suitable fitting result for the majority of cases.

Since droplet height is non-negligible when estimating surface energy under small Weber numbers ($We \leq 30$), we safely move on to the investigation of the correlation between droplet height and the surface area. As discussed in Figure 12, droplet deformation and its transition can be characterized by three distinct heights, namely, the center height h_c, the throat height h_t and the rim height h_r. To simplify the quantification on surface energy, droplet at τ_{max} can be equivalent to a "column-shaped" cylinder with the identical droplet maximum spreading diameter D_{max} and surface energy. Therefore, droplet height characterization can be simplified by using an equivalent surface energy height h_e, in this case surface energy can be expressed as

$$E_s(\tau_m) = \sigma\pi\left[D_m h_e + \frac{D_m^2(1 - cos\theta)}{4}\right] \tag{8}$$

where θ is the contract angle and can be determined as 180° in our simulations, as discussed in section III A. h_e can be further normalized by the D_{max} as $R_e = h_e / D_{max}$, which measures the relative importance of droplet height when compared to the droplet spreading diameter, and we found that R_e is related to droplet impact inertia, as shown in Figure 14 that,

$$R_e = 0.1We_r^{-0.4} \tag{9}$$

Consequently, β_{max} can be estimated by accounting for droplet surface energy increment at τ_{max}, yields

$$\beta_{max} = \sqrt{\frac{0.7We_r^{0.9} + 0.1}{0.1We_r^{-0.4} + (1 - cos\theta)/4}} \left(\text{Free-slip}, We \le 30\right) \tag{10}$$

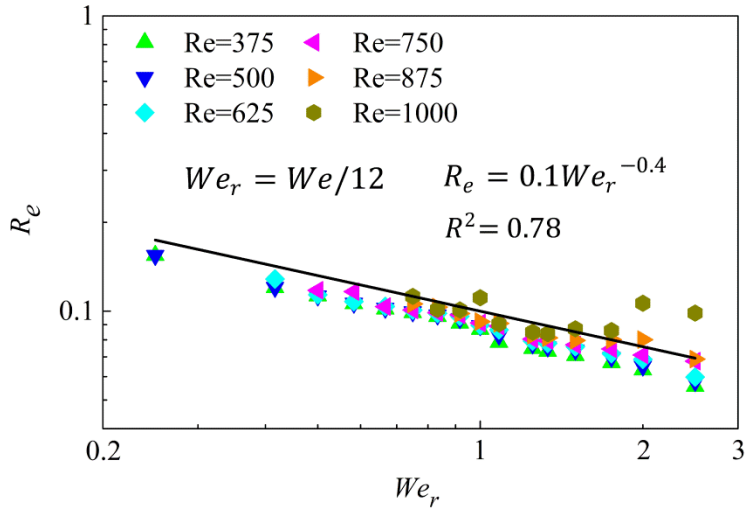

Figure 14. Correlation between the normalized droplet equivalent height $R_e = h_e/D_{max}$ and revised Weber number We_r with $R^2 = 0.78$.

Figure 15 shows the comparison among the present model (i.e., equation 10, denoted by the red line), the available numerical predictions and various experimental results. Following Lastakowski et al. [59], the droplet spreading on the free-slip surface with a gas film that existed throughout the whole spreading process can be regarded as a result of the impacts of Leidenfrost droplet. We therefore employed Pan et al.'s experimental results [54] of equal droplet collision, Tang et al.'s [11] experimental results of equal droplet collision and Tran et al.'s experimental results of Leidenfrost droplet in this comparison to validate the proposed model. Serval observations can be made in this figure as follows. Firstly, our numerical predictions agree well with these experimental data, which again confirms the accuracy of the present simulation. Secondly, the derived model for estimating β_{max} under small Weber numbers ($We \le 30$) shows good agreement with both these experimental results and our numerical predictions. Finally, the present model and Wildeman et al.'s model shows fine continuity at $We = 30$. It is worth noting that the model proposed in the current work is based on a contact angle of 180° for droplet spreading and there is also a good agreement with the results of our experimental results with variable advancing contact angle around 180°.

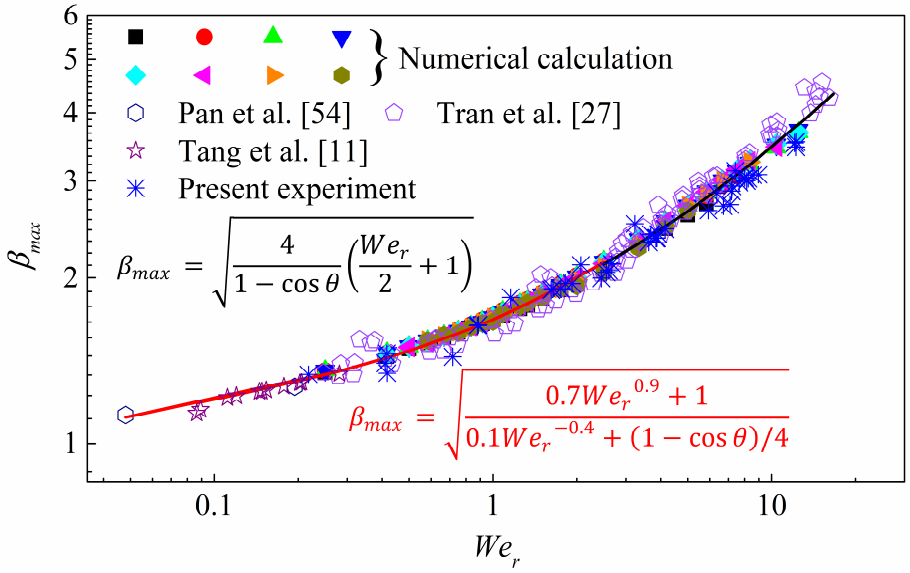

Figure 15. Comparison between the derived spreading models (black solid line indicates Wildeman et al.'s model [40], while the red line denotes the present proposed model) and data points (Tang et al.'s experimental results (denoted by the pentagram symbols) [11], Tran et al.'s experimental results (denoted by the pentagon symbols) [27], Pan et al.'s experimental results (denoted by the hexagon symbols) [54], present experiment and numerical predictions).

4. Conclusions

A comprehensive experimental and numerical study on droplet impacts on a free-slip surface is presented in this study, with particular emphasis on the dynamics under small Weber numbers ($We \leq 30$) and different impacting parameters.

Our experimental and numerical results for large Weber numbers ($We > 30$) show good agreement with the prediction of the widely-used model of Wildeman et al. wherein the simulation successfully predicted the "1/2 rule" for the reliable dimensionless droplet maximum spreading diameter β_{max}. Moreover, our numerical prediction of a relationship between β_{max} and spreading time τ_{max} agrees well with the previous investigation [40]. In terms of the spreading under relatively small Weber numbers ($We \leq 30$), we found β_{max} deviates from Wildeman et al.'s [40] model for the following two reasons. Firstly, as droplet impact inertia decreases to $We \leq 30$, where a We-dependent energy budget can be found, the "1/2 rule" breaks down. Secondly, droplet progressively lost its thin pizza-like shape and finally degenerated into puddle-like shape whose height is non-negligible when estimating the surface energy.

Droplet spreading can be divided into three distinct regimes. The first regime (I) is characterized by the puddle-shaped droplet at τ_{max}, in this case initial kinetic energy is insufficiently strong to overcome the surface tension force, hence droplet surface energy dominates energy budget, restricts droplet deformation, and therefore produces a similar strain rate. Consequently, viscous dissipation in regime (I) is controlled by the liquid viscosity (denoted by Re) and decreases as Re increases. The second regime (II) is regarded as the transition regime. In this case, initial kinetic energy is comparable to the surface energy so that surface energy dominates the energy budget when the initial kinetic energy can be consumed in a timely manner at the earlier stage, probably under relatively small Re cases; while kinetic energy in turn dominates the energy budget under the condition of relatively large Re cases, because the unconsumed kinetic energy is sufficiently strong to overcome the surface tension force. The competition between surface energy and kinetic energy finally results in the dual role of liquid viscosity and therefore a non-monotonic energy budget. The third regime (III) is characterized by the uniform droplet deformation (thin pizza-shaped), where initial kinetic energy is far stronger than the surface

energy so that it dominates the energy budget, resulting in the "1/2 rule" being validated and droplet height being negligible when compared to the spreading diameter.

Based on the understanding of droplet spreading under small Weber numbers ($We \leq 30$), the energy conservation approach was again employed to model the dimensionless droplet maximum spreading diameter β_{max} by accounting for the influence of impact parameters (such as We and Re) on the energy budget and the droplet height at τ_{max}. A revised Weber number We_r, which correctly reflects the orders of magnitude of various energies, was adopted to replace the We in our modeling works. The proposed model was found to correlate well with the numerical results and the experimental results of Pan et al. [54], Tang et al., Tran et al. and our present experiment, it can therefore be expressed as a practical model to estimate β_{max} under smaller Weber numbers ($We \leq 30$).

Author Contributions: Conceptualization, Z.Z.; methodology, N.W.; software, Z.Z.; validation, N.W.; formal analysis, N.W.; investigation, N.W.; resources, J.Z.; data curation, N.W.; writing—original draft preparation, N.W.; writing—review and editing, Z.Z.; visualization, N.W.; supervision, Z.Z.; project administration, J.Z.; funding acquisition, J.Z. All authors have read and agreed to the published version of the manuscript.

Funding: This research was funded by National Natural Science Foundation of China grant number 51806013, Foundation research funds of Ministry of Industry and Information Technology grant number JCKY2019602D018 and Beijing Institute of Technology Research Fund Program for Young Scholars grant number 2020CX04047. The APC was funded by National Natural Science Foundation of China grant number 51806013.

Data Availability Statement: The dataset used and/or analyzed during the current study is available from the corresponding author.

Acknowledgments: The authors would like to thank the reviewers for their valuable comments and the administrative staff.

Conflicts of Interest: The authors declare no conflict of interest.

References

1. Yarin, A.L. DROP IMPACT DYNAMICS: Splashing, Spreading, Receding, Bouncing…. *Annu. Rev. Fluid Mech.* **2006**, *38*, 159–192. https://doi.org/10.1146/annurev.fluid.38.050304.092144.
2. Ezzatneshan, E.; Khosroabadi, A. Droplet spreading dynamics on hydrophobic textured surfaces: A lattice Boltzmann study. *Comput. Fluids* **2021**, *231*, 105063. https://doi.org/10.1016/j.compfluid.2021.105063.
3. Banitabaei, S.A.; Amirfazli, A. Droplet impact onto a solid sphere in mid-air: Effect of viscosity, gas density, and diameter ratio on impact outcomes. *Phys. Fluids* **2020**, *32*, 037102. https://doi.org/10.1063/1.5139057.
4. Sun, T.P.; Alvarez-Novoa, F.; Andrade, K.; Gutierrez, P.; Gordillo, L.; Cheng, X. Stress distribution and surface shock wave of drop impact. *Nat. Commun.* **2022**, *13*, 1703. https://doi.org/10.1038/s41467-022-29345-x.
5. Ju, J.; Yang, Z.; Yi, X.; Jin, Z. Experimental investigation of the impact and freezing processes of a hot water droplet on an ice surface. *Phys. Fluids* **2019**, *31*, 057107. https://doi.org/10.1063/1.5094691.
6. Zhang, J.T.; Liu, H.R.; Ding, H. Head-on collision of two immiscible droplets of different components. *Phys. Fluids* **2020**, *32*, 082106. https://doi.org/10.1063/5.0018391.
7. Ezzatneshan, E.; Goharimehr, R. Study of spontaneous mobility and imbibition of a liquid droplet in contact with fibrous porous media considering wettability effects. *Phys. Fluids* **2020**, *32*, 113303. https://doi.org/10.1063/5.0027960.
8. Wu, H.; Zhang, F.; Zhang, Z. Droplet breakup and coalescence of an internal-mixing twin-fluid spray. *Phys. Fluids* **2021**, *33*, 013317. https://doi.org/10.1063/5.0030777.
9. Liu, X.; Zhang, X.; Min, J. Maximum spreading of droplets impacting spherical surfaces. *Phys. Fluids* **2019**, *31*, 092102. https://doi.org/10.1063/1.5117278.
10. Lamanna, G.; Geppert, A.; Bernard, R.; Weigand, B. Drop impact onto wetted walls: An unsteady analytical solution for modelling crown spreading. *J. Fluid Mech.* **2022**, *938*, A34. https://doi.org/10.1017/jfm.2022.69.
11. Tang, C.; Qin, M.; Weng, X.; Zhang, X.; Zhang, P.; Li, J.; Huang, Z. Dynamics of droplet impact on solid surface with different roughness. *Int. J. Multiphase Flow* **2017**, *96*, 56–69. https://doi.org/10.1016/j.ijmultiphaseflow.2017.07.002.
12. Moreira, A.L.N.; Moita, A.S.; Panão, M.R. Advances and challenges in explaining fuel spray impingement: How much of single droplet impact research is useful? *Prog. Energy Combust. Sci.* **2010**, *36*, 554–580. https://doi.org/10.1016/j.pecs.2010.01.002.
13. de Goede, T.; de Bruin, K.; Shahidzadeh, N.; Bonn, D. Droplet splashing on rough surfaces. *Phys. Rev. Fluids* **2021**, *6*, 043604. https://doi.org/10.1103/PhysRevFluids.6.043604.

14. Bouillant, A.; Lafoux, B.; Clanet, C.; Quere, D. Thermophobic Leidenfrost. *Soft Matter* **2021**, *17*, 8805–8809. https://doi.org/10.1039/d1sm00548k.
15. García-Geijo, P.; Quintero, E.S.; Riboux, G.; Gordillo, J.M. Spreading and splashing of drops impacting rough substrates. *J. Fluid Mech.* **2021**, *917*, A50. https://doi.org/10.1017/jfm.2021.313.
16. Bennett, T.; Poulikakos, D. Splat-quench solidification-estimating the maximum spreading of a droplet impacting a solid surface. *J. Mater. Sci.* **1993**, *28*, 963–970.
17. German, G.; Bertola, V. Review of drop impact models and validation with high-viscosity Newtonian fluids. *Atom. Sprays* **2009**, *19*, 787–807. https://doi.org/10.1615/AtomizSpr.v19.i8.60.
18. Marengo, M.; Antonini, C.; Roisman, I.V.; Tropea, C. Drop collisions with simple and complex surfaces. *Curr. Opin. Colloid Interface Sci.* **2011**, *16*, 292–302. https://doi.org/10.1016/j.cocis.2011.06.009.
19. Scheller, B.L.; Bousfield, D.W. Newtonian drop impact with a solid surface. *AlChE J.* **1995**, *41*, 1357–1367.
20. Marmanis, H.; Thoroddsen, S.T. Scaling of the fingering pattern of an impacting drop. *Phys. Fluids* **1996**, *8*, 1344–1346. https://doi.org/10.1063/1.868941.
21. Weiss, D.A.; Yarin, A.L. Single drop impact onto liquid films- Neck distortion, jetting, tiny bubble entrainment, and crown formation. *J. Fluid Mech.* **1999**, *385*, 229–254. https://doi.org/10.1017/S002211209800411X.
22. Rioboo, R.; Marengo, M.; Tropea, C. Outcomes from a drop impact on solid surface. *Atom. Sprays* **2001**, *11*, 155–166.
23. Clanet, C.; BÉGuin, C.; Richard, D.; QuÉRÉ, D. Maximal deformation of an impacting drop. *J. Fluid Mech.* **2004**, *517*, 199–208. https://doi.org/10.1017/s0022112004000904.
24. Bayer, I.S.; Megaridis, C.M. Contact angle dynamics in droplets impacting on flat surfaces with different wetting characteristics. *J. Fluid Mech.* **2006**, *558*, 415–449. https://doi.org/10.1017/s0022112006000231.
25. Bejan, A.; Gobin, D. Constructal theory of droplet impact geometry. *Int. J. Heat Mass Transfer* **2006**, *49*, 2412–2419. https://doi.org/10.1016/j.ijheatmasstransfer.2006.02.001.
26. Eggers, J.; Fontelos, M.A.; Josserand, C.; Zaleski, S. Drop dynamics after impact on a solid wall: Theory and simulations. *Phys. Fluids* **2010**, *22*, 062101. https://doi.org/10.1063/1.3432498.
27. Tran, T.; Staat, H.J.J.; Prosperetti, A.; Sun, C.; Lohse, D. Drop Impact on Superheated Surfaces. *Phys. Rev. Lett.* **2012**, *108*, 036101. https://doi.org/10.1103/PhysRevLett.108.036101.
28. Laan, N.; de Bruin, K.G.; Bartolo, D.; Josserand, C.; Bonn, D. Maximum Diameter of Impacting Liquid Droplets. *Phys. Rev. Appl.* **2014**, *2*, 044018. https://doi.org/10.1103/PhysRevApplied.2.044018.
29. Seo, J.; Lee, J.S.; Kim, H.Y.; Yoon, S.S. Empirical model for the maximum spreading diameter of low-viscosity droplets on a dry wall. *Exp. Therm. Fluid Sci.* **2015**, *61*, 121–129. https://doi.org/10.1016/j.expthermflusci.2014.10.019.
30. Davidson, M.R. Spreading of an inviscid drop impacting on a liquid film. *Chem. Eng. Sci.* **2002**, *57*, 3639–3647.
31. Roisman, I.V.; Rioboo, R.; Tropea, C. Normal Impact of a Liquid Drop on a Dry Surface- Model for Spreading and Receding. *Proc. R. Soc. A-Math. Phys. Eng. Sci.* **2002**, *458*, 1411–1430.
32. Roisman, I.V.; Berberović, E.; Tropea, C. Inertia dominated drop collisions. I. On the universal flow in the lamella. *Phys. Fluids* **2009**, *21*, 052103. https://doi.org/10.1063/1.3129282.
33. Roisman, I.V. Inertia dominated drop collisions. II. An analytical solution of the Navier–Stokes equations for a spreading viscous film. *Phys. Fluids* **2009**, *21*, 052104. https://doi.org/10.1063/1.3129283.
34. Chandra, S.; Avedisian, C.T. On the Collision of a Droplet with a Solid Surface. *Proc. R. Soc. A-Math. Phys. Eng. Sci.* **1998**, *432*, 13–41.
35. Fukai, J.; Shiiba, Y.; Yamamoto, T.; Miyatake, O.; Poulikakos, D.; Megaridis, C.M.; Zhao, Z. Wetting effects on the spreading of a liquid droplet colliding with a flat surface: Experiment and modeling. *Phys. Fluids* **1995**, *7*, 236–247. https://doi.org/10.1063/1.868622.
36. Pasandideh-Fard, M.; Qiao, Y.M.; Chandra, S.; Mostaghimi, J. Capillary effects during droplet impact on a solid surface. *Phys. Fluids* **1996**, *8*, 650–659. https://doi.org/10.1063/1.868850.
37. Fukai, J.; Tanaka, M.; Miyatake, O. Maximum Spreading of Liquid Droplets Colliding with Flat Surfaces. *J. Chem. Eng. Jpn.* **2004**, *31*, 456–461. https://doi.org/10.1252/jcej.31.456.
38. Attané, P.; Girard, F.; Morin, V. An energy balance approach of the dynamics of drop impact on a solid surface. *Phys. Fluids* **2007**, *19*, 012101. https://doi.org/10.1063/1.2408495.
39. An, S.M.; Lee, S.Y. Maximum spreading of a shear-thinning liquid drop impacting on dry solid surfaces. *Exp. Therm Fluid Sci.* **2012**, *38*, 140–148. https://doi.org/10.1016/j.expthermflusci.2011.12.003.
40. Wildeman, S.; Visser, C.W.; Sun, C.; Lohse, D. On the spreading of impacting drops. *J. Fluid Mech.* **2016**, *805*, 636–655.
41. Gao, S.; Liao, Q.; Liu, W.; Liu, Z. Nanodroplets Impact on Rough Surfaces: A Simulation and Theoretical Study. *Langmuir* **2018**, *34*, 5910–5917. https://doi.org/10.1021/acs.langmuir.8b00480.
42. Park, S.W.; Lee, C.S. Macroscopic and microscopic characteristics of a fuel spray impinged on the wall. *Exp. Fluids* **2004**, *37*, 745–762. https://doi.org/10.1007/s00348-004-0866-3.
43. Qin, M.; Tang, C.; Tong, S.; Zhang, P.; Huang, Z. On the role of liquid viscosity in affecting droplet spreading on a smooth solid surface. Int. J. Multiph. Flow 2019, 117, 53–63. https://doi.org/10.1016/j.ijmultiphaseflow.2019.05.002.
44. Zhang, Z.; Zhang, P. Numerical Interpretation to the Roles of Liquid Viscosity in Droplet Spreading at Small Weber Numbers. *Langmuir* **2019**, *35*, 16164–16171. https://doi.org/10.1021/acs.langmuir.9b02736.

45. Huang, H.-M.; Chen, X.-P. Energetic analysis of drop's maximum spreading on solid surface with low impact speed. *Phys. Fluids* **2018**, *30*, 022106. https://doi.org/10.1063/1.5006439.
46. Wang, F.; Yang, L.; Wang, L.; Zhu, Y.; Fang, T. Maximum Spread of Droplet Impacting onto Solid Surfaces with Different Wettabilities: Adopting a Rim-Lamella Shape. *Langmuir* **2019**, *35*, 3204–3214. https://doi.org/10.1021/acs.langmuir.8b03748.
47. Zhang, Z.; Zhang, P. Kinetic energy recovery and interface hysteresis of bouncing droplets after inelastic head-on collision. *Phys. Fluids* **2017**, *29*, 103306. https://doi.org/10.1063/1.5000547.
48. Zhang, Z.; Zhang, P. Modeling Kinetic Energy Dissipation of Bouncing Droplets for Lagrangian Simulation of Impinging Sprays Under High Ambient Pressures. *Atom. Sprays* **2018**, *28*, 673–694.
49. Unverdi, S.O.; Tryggvason, G. A front-tracking method for viscous, incompressible, multi-fluid flows. *J. Comput. Phys.* **1992**, *100*, 25–37.
50. Tryggvason, G.; Bunner, B.; Esmaeeli, A.; Juric, D.; Al-Rawahi, N.; Tauber, W.; Han, J.; Nas, S.; Jan, Y.J. A Front-Tracking Method for the Computations of Multiphase Flow. *J. Comput. Phys.* **2001**, *169*, 708–759. https://doi.org/10.1006/jcph.2001.6726.
51. Nobari, M.R.H.; Jan, Y.J.; Tryggvason, G. Head-on collision of drops—A numerical investigation. *Phys. Fluids* **1993**, *8*, 29–42.
52. Qian, J.; Law, C.K. Regimes of coalescence and separation in droplet collision. *J. Fluid Mech.* **1997**, *331*, 59–80.
53. Singh, R.; Shyy, W. Three-dimensional adaptive Cartesian grid method with conservative interface restructuring and reconstruction. *J. Comput. Phys.* **2007**, *224*, 150–167. https://doi.org/10.1016/j.jcp.2006.12.026.
54. Pan, K.L.; Law, C.K.; Zhou, B. Experimental and mechanistic description of merging and bouncing in head-on binary droplet collision. *J. Appl. Phys.* **2008**, *103*, 064901. https://doi.org/10.1063/1.2841055.
55. Pan, K.L.; Yin, G.C. Parallel strategies of front-tracking method for simulation of multiphase flows. *Compute. Fluids* **2012**, *67*, 123–129. https://doi.org/10.1016/j.compfluid.2012.07.010.
56. Kuan, C.K.; Pan, K.L.; Shyy, W. Study on high-Weber-number droplet collision by a parallel, adaptive interface-tracking method. *J. Fluid Mech.* **2014**, *759*, 104–133. https://doi.org/10.1017/jfm.2014.558.
57. Zhang, P.; Law, C.K. An analysis of head-on droplet collision with large deformation in gaseous medium. *Phys. Fluids* **2011**, *23*, 042102. https://doi.org/10.1063/1.3580754.
58. Pan, K.L.; Chou, P.C.; Tseng, Y.J. Binary droplet collision at high Weber number. *Phys. Rev. E Stat. Nonlin. Soft Matter Phys.* **2009**, *80*, 036301. https://doi.org/10.1103/PhysRevE.80.036301.
59. Lastakowski, H. Drop Impacts on air Cushions: Super-Hydrophobic, Hot or Moving Surfaces. Ph.D. Thesis, Institut Lumière Matière, Ville-urbanne CEDEX, France, 2013.